Supplemental Document

Dynamics of optical vortices in van der Waals materials: supplement

YANIV KURMAN,[1] RAPHAEL DAHAN,[1] HANAN HERZIG SHENFUX,[2] GILLES ROSOLEN,[3] ELI JANZEN,[4] JAMES H. EDGAR,[4] FRANK H. L. KOPPENS,[2,5] AND IDO KAMINER[1,*]

[1]*Department of Electrical Engineering, Technion - Israel Institute of Technology, 32000 Haifa, Israel*
[2]*ICFO-Institut de Ciències Fotòniques, The Barcelona Institute of Science and Technology, Av. Carl Friedrich Gauss 3, 08860 Castelldefels (Barcelona), Spain*
[3]*Micro and Nanophotonic Materials Group, Research Institute for Materials Science and Engineering, University of Mons, 7000 Mons, Belgium*
[4]*Tim Taylor Department of Chemical Engineering, Kansas State University, Manhattan, Kansas 66506, USA*
[5]*ICREA-Institució Catalana de Recerca i Estudis Avanats, Passeig Lluís Companys 23, 08010 Barcelona, Spain*
[*]*kaminer@technion.ac.il*

Supplement DOI: https://doi.org/10.6084/m9.figshare.22683274

Parent Article DOI: https://doi.org/10.1364/OPTICA.485120

Dynamics of optical vortices in van der Waals materials

Yaniv Kurman[1], Raphael Dahan[1], Hanan Herzig Shenfux[2], Gilles Rosolen[3], Eli Janzen[4], James H. Edgar[4], Frank H. L. Koppens[2,5], and Ido Kaminer[1*]

[1]Department of Electrical Engineering, Technion, Israel Institute of Technology, 32000 Haifa, Israel

[2]ICFO-Institut de Ciències Fotòniques, The Barcelona Institute of Science and Technology, Av. Carl Friedrich Gauss 3, 08860 Castelldefels (Barcelona), Spain

[3]Micro and Nanophotonic Materials Group, Research Institute for Materials Science and Engineering, University of Mons, 7000 Mons, Belgium

[4]Tim Taylor Department of Chemical Engineering, Kansas State University, Manhattan, KS 66506 USA

[5]ICREA-Institució Catalana de Recerca i Estudis Avanats, Passeig Lluís Companys 23, 08010 Barcelona, Spain

Supplementary Materials

Contents

S1. Experimental setup – the ultrafast electron microscope

To image the spatiotemporal dynamics of the PhPs and their vortices, we used an ultrafast transmission electron microscope (UTEM). The UTEM is a pump–probe setup based on a JEOL JEM-2100 Plus TEM with a LaB_6 electron gun, which we operated at acceleration voltage 200 kV. The imaging is driven by a 40 Watt, 1030 nm laser (Carbide, Light Conversion) with pulse duration ~270 fs, operating at a 1 MHz repetition rate. Each pulse splits into two pulses using a beam splitter. One pulse (probe) undergoes two stages of second-harmonic generation, converted into ultraviolet (UV) and excites the electron probe inside the TEM using the photoelectric effect. The second pulse (pump) enters an optical parametric amplifier (OPA, Light Conversion Orpheus) and is converted to the IR through a difference frequency generation (DFG) process. The delay τ_d between the electron probe and the IR pump is controlled by a motorized stage.

The temporal profile of the laser pulse is characterized through an independent PINEM measurement on a metallic film, showing a FWHM of 0.6 ps. A spectral measurement was acquired through a Michelson interferometer near the DFG, showing an excitation peak frequency of 7.25 μm. This laser beam arrives via side illumination, perpendicular to the direction of motion of the electron (z). The laser's spot size is ~30 μm which is significantly larger than the sample size, with average power between 80 to 100 mW (fluence of $\sim 2\frac{\mathrm{mJ}}{(\mathrm{cm})^2}$). To prevent shadowing of the laser by the TEM grid and holder, our sample was tilted at an angle of 20^o. We note that after the initial pulse excitation is over, the contribution of non-PhP fields to our measurement is negligible.

To produce the energy-filtered transmission electron microscopy (EFTEM) images, we used electron beams with a zero-loss peak (ZLP) of 0.9 eV prior to the interaction. These electrons reach the sample with a beam radius of 20 μm, which covers the entire sample. The entire frame had dimensions of 35×35 μm^2, to reduce isochromaticity effects within the sample (reaching pixel resolution of 34.1×34.1 nm^2). After the interaction of the free electrons with the excited sample, they undergo an energy filtering so that the image includes only the electrons that gained between 1.5 eV to 4.5 eV. The free electron energy spectrum is measured in a post-column EELS system with a spectrometer dispersion of ~0.1 eV (Gatan). The choice of the filtering values also reduced the sensitivity to the zero-loss peak drift during the measurement. The slit creates a nonlinear relation between the electron signal and the electric field due to a sharp threshold below which the

electric field cannot be measured. The minimal electron energy gain in our slit, 1.5 eV, correspond to an approximate electric field threshold of 1 MV/m (calculation can be found in (*1*)). The exposure time for each frame was 100 seconds (overall 2 hours and 35 minutes for the entire measurement).

The probing of the PhPs by free electrons is based on the PINEM interaction (*2*, *3*). The coupling strength g between the electron and the electric field of frequency ω in the sample is described by

$$g(\omega,x,y) = \frac{e}{\omega\hbar}\int_{-\infty}^{\infty} dz\, E_z(x,y,z,\omega)e^{-i\frac{\omega}{v}z}, \#(S1)$$

where e and v are the electron charge and velocity, respectively, $\hbar$ is the reduced Planck's constant, and the z axis is aligned to the electron trajectory. Therefore, at each transverse position (x,y), the electron experiences a different coupling strength from which the PhP field is extracted. The signature of the coupling strength on the electron is a change in the electron energy loss spectrum (EELS), where the electron can emit or absorb n quanta of light with different probabilities due to a stimulated emission process. Overall, the probability for the free electron to change its energy by ΔE after the interaction is $\mathrm{EELS}(\Delta E,x,y) = \rho_{ZLP}(\Delta E) * \sum_n \left|J_n\left(2\int d\omega g(\omega,x,y)\right)\right|^2 \delta(\Delta E - n\hbar\omega)$, with J_n being the Bessel function and $\rho_{ZLP}(\Delta E)$ the zero-loss-peak probability density that describes the pre-interaction electron. For more details regarding the broadband excitation, see (*1*, *4*). Importantly, although the sample is tilted, and the electron does not probe exactly the E_z field that we simulated, the small tilt that we used does not affect the observation of the vortices since the vortices appear also for the electric fields parallel to the sample. Nevertheless, we note that a larger tilt could affect the measurement due to evanescent fields from different sides of the vortex, which would require a more advanced analysis for extracting the vortices.

S2. Simulating the spatiotemporal dynamics of phonon-polariton vortices

In this section, we present the modeling of the time evolution of PhP vortices. Briefly, to calculate the vortex dynamics, we first convert the laser excitation to the frequency domain, with each frequency component inducing a set of dipoles along the edges of the sample (*5*). The relative phase and orientation of each dipole follows the laser's polarization and propagation direction. We then find the PhP electric field pattern each dipole creates using the dyadic Green's function of a 40 nm hBN sheet and the added phases due to reflection from the edges (*6*, *7*). The total frequency response is the sum of all dipole contributions, and thus the total time response is its Fourier transform (i.e., a superposition of PhP frequency responses). Using this method for different laser properties and on different sample geometries allows us to identify the key features found in the measured data. This approach finds the evolution in time of the PhP field amplitude and phase, which incorporate the vortices.

Consider a single-frequency plane wave exciting a set of dipoles along the edge of the sample. The incoming plane wave has the following electric field:

$$\boldsymbol{E}_{\mathrm{in}}(\boldsymbol{r},\omega) = E_0\left(\cos(\alpha)\,\hat{\boldsymbol{\varepsilon}}_{\mathbf{1}} + e^{i\beta}\sin(\alpha)\,\hat{\boldsymbol{\varepsilon}}_{\mathbf{2}}\right)e^{-i\frac{\omega}{c}\left(\sin(\theta)\cos(\varphi)\,x+\sin(\theta)\sin(\varphi)\,y-\cos(\theta)\,z\right)} \quad \#(\mathrm{S2})$$

where θ is the propagation angle compared to the z axes, and φ is the angle compared to the x axes. The polarizations are $\hat{\boldsymbol{\varepsilon}}_{\mathbf{1}} = \sin(\varphi)\hat{\boldsymbol{x}} - \cos(\varphi)\hat{\boldsymbol{y}}$ and $\hat{\boldsymbol{\varepsilon}}_{\mathbf{2}} = \cos(\theta)\cos(\varphi)\hat{\boldsymbol{x}} + \cos(\theta)\sin(\varphi)\hat{\boldsymbol{y}} + \sin(\theta)\hat{\boldsymbol{z}}$. We note that the phase of the field breaks the square symmetry is our simulations. Notably, these polarizations cannot be addressed completely as TE and TM since there is no translational symmetry in any of the directions. As a result, both polarizations can excite the TM polarized PhPs.

The TM polarization of the PhPs means that they can only be excited by dipoles perpendicular to the edge. That is, by assuming a linear polarizability α and an edge along the y-axis, the induced dipole along the edge is written as $\boldsymbol{p}_{\mathrm{in}} = \alpha[(\boldsymbol{E}_{\mathrm{in}}(y)\cdot\hat{\boldsymbol{x}})\hat{\boldsymbol{x}} + (\boldsymbol{E}_{\mathrm{in}}(y)\cdot\hat{\boldsymbol{z}})\hat{\boldsymbol{z}}\,]$. From Eq. (S1), we find the relative phase between the dipoles along the edge of the sample, shown in Fig. S5d. In the same figure, we also show the direction of the dipoles in each one of the edges, as determined by the excitation properties.

The exact strength of each dipole α does not have a simple analytical expression (although the maximal coupling was investigated (*5*)). We find it sufficient to use the scaling of the polarizability, being proportional to λ_p^2/λ_0^2 (where λ_p and λ_0 are the polariton and free-space

wavelengths). This scaling agrees with the intuition that a larger momentum mismatch is more easily overcome when the plasmonic wavelength is smaller.

Next, we connect between the dipoles and the PhP electric field that is produced in the sample. For a set of dipoles, this connection is done using the Dyadic Green's function $\overleftrightarrow{G}$, through

$$\boldsymbol{E}_{\mathrm{php}}(\boldsymbol{r};\omega) = \int \mathrm{d}\boldsymbol{r_s}\overleftrightarrow{G}(\boldsymbol{r};\boldsymbol{r_s};\omega)\boldsymbol{p}_{\mathrm{in}}(\boldsymbol{r_s};\omega)\ . \#(S3)$$

For an infinite slab, the Green's function component that excites E_z takes the form of

$$G_{zx}^{\mathrm{inf}}(x,y,z=0,x_s,y_s,z'=0;\omega) = \frac{ic^2}{8\pi^2\omega^2}\int_{-\infty}^{\infty}\int_{-\infty}^{\infty} dq_x\, dq_y q_x e^{-iq_y(y-y_s)}e^{-iq_x(x-x_s)}r_p(q,\omega)$$

$$G_{zy}^{\mathrm{inf}}(x,y,z=0,x_s,y_s,z'=0;\omega) = \frac{ic^2}{8\pi^2\omega^2}\int_{-\infty}^{\infty}\int_{-\infty}^{\infty} dq_x\, dq_y q_y e^{-iq_y(y-y_s)}e^{-iq_x(x-x_s)}r_p(q,\omega)$$

$$G_{zz}^{\mathrm{inf}}(x,y,z=0,x_s,y_s,z'=0;\omega) = \frac{ic^2}{8\pi^2\omega^2}\int_{-\infty}^{\infty}\int_{-\infty}^{\infty} dq_x\, dq_y \frac{q^2}{k_z} e^{-iq_y(y-y_s)}e^{-iq_x(x-x_s)}r_p(q,\omega)$$

where c is the speed of light in vacuum and $k_z = \sqrt{\frac{\omega^2}{c^2} - q^2}$. The p-polarized reflection coefficient of the hBN slab $r_p(q,\omega)$ is a function of in-plane momentum $q = \sqrt{q_x^2 + q_y^2}$ and frequency ω, incorporating the dispersion of the PhP (shown in Fig. S5a). These Green's functions convert the dispersion in momentum space to spatial responses which are drawn in Fig. S5b. For a finite slab, the Green's function also includes the reflections from the edges. For an excitation along one of the x-edges (constant x_s), we can write

$$\overleftrightarrow{G}^{\mathrm{fin}}(\boldsymbol{r};\boldsymbol{r_s};\omega) = \sum_{j_x=0}^{\infty}\sum_{j_y=\infty}^{\infty} e^{\frac{i\pi}{4}(j_x+|j_y|)}\overleftrightarrow{G}^{\mathrm{inf}}\big((-1)^j x + j_x L_x,(-1)^j y + j_y L_y,z=0,x_s,y_s,z_s=0;\omega\big) \#(S4)$$

where we used the anomalous reflection of $\pi/4$ and defined the sample's x and y dimensions L_x and L_y, respectively. As an example, $\overleftrightarrow{G}_{zx}^{\mathrm{fin}}(\boldsymbol{r};\boldsymbol{r_s};\omega)$ for a dipole located at a specific location along the edge is plotted in Fig. S5c.

When combining the excitation properties with the Green's function response, we can find the PhP field for a specific frequency $\boldsymbol{E}_{\mathrm{php}}(\boldsymbol{r};\omega)$, as shown in Figs. S5e-f. Finally, we describe the temporal field of the PhP as a Fourier transform of its frequency counterpart:

$$\boldsymbol{E}_{\mathrm{php}}(x,y;t) = \mathcal{F}^{-1}\{\boldsymbol{E}_{\mathrm{php}}(\boldsymbol{r};\omega)\} = \mathcal{F}^{-1}\Big\{\int \mathrm{d}\boldsymbol{r_s}\overleftrightarrow{G}^{\mathrm{fin}}(\boldsymbol{r};\boldsymbol{r_s};\omega)\alpha\mathcal{F}\{\boldsymbol{E}_{\mathrm{in}}(\boldsymbol{r_s};t)\}\Big\}. \#(S5)$$

Using Eq. 4, we translate the temporal shape of the incoming laser excitation into the temporal dynamics of the PhP. In our simulations, we concentrate on the z component of the PhP field

because the electron is sensitive only to that field polarization. We analyze both the amplitude and the phase of $\boldsymbol{E}_{\mathrm{php}}$ to identify the vortices and follow their dynamics.

S3. Sample preparation and analysis

The isotopically pure $h^{10}BN$ crystal was grown at atmospheric pressure from an iron solvent using the process described in Ref. (*8*). Then, they were mechanically exfoliated in a dry transfer directly on viscoelastic polydimethylsiloxane (PDMS) tapes (GELPAK). The exfoliated sample was then transferred to a 19.5 nm Si_3N_4 membrane (Norcada). The exact exfoliation subtle stages, including the required temperatures, are the same as in Ref. (*1*). We have analyzed the cleanliness of the sample and determined its thickness using an FEI Titan Themis G2 TEM with acceleration voltage of 200 kV, see Fig. S3. Using a high-resolution imaging, we detected the hBN hexagonal lattice (Fig. S3b) and its Fourier transform (Fig. S3c). Using this imaging, we analyzed the surface quality of the sample.

To further analyze the quality, and extract the thickness of the sample, we have used the EELS log ratio measurement. This process requires taking two images: the first is an unfiltered image that includes the electron with all energy losses (I, Fig. S3d) and the second is a filtered image that includes only the electrons that remained in the zero-loss peak, i.e., the electrons that did not encounter elastic scattering (I_0, Fig. S3e). Then, the ratio $\log(I_0/I)$ equals the ratio between the thickness of the sample t and the electron mean-free-path inside the material λ (Fig. S3f). To find the thickness of the $h^{10}BN$ sample, we first use this method to find the thickness of the Si_3N_4 when substituting $\lambda_{\mathrm{SiN}} = 88.1$ nm (*9*). This way we verify that the membrane thickness is 19.531 ± 0.0015 nm. After reducing the membrane's t/λ, we find that the main area of the $h^{10}BN$ is 40.3 ± 0.22 nm (using $\lambda = 128$ nm(*10*)). However, there are areas which are significantly thicker as a round area of 53 ± 0.6 nm, a thick line of 110 ± 5 nm, and thin areas near parts of the edges with 22 ± 5 nm. These defects might create additional vortex-type effects that disagree with our simulations, see section S4 below for a further discussion.

S4. PhP ring shape

We identified in the measurements a field shape which was not seen in the simulation: rings of PhP field, see Fig. S8. According to our vortex analysis, a peak of the field is created when it is surrounded by vortices of alternating signs. Such a peak is conserved as long as the surrounding vortices keep their locations, since all the area within needs to remain with the same phase. However, we find cases in which the peak is not conserving its shape. The surrounding vortices maintain their locations, though the amplitude in the center of the peak is decreasing. Since this amplitude is not zero, we cannot claim that vortices were created there, although the signature of a vortex pair seems to appear and then vanish.

We analyzed several suggestions for explaining the effect. The first option is having height defects in the sample (shown in Fig. S8 above). We know that defects can create vortices (*11*), but it does not explain why these created vortices remain static in space and do not show a zero amplitude. A second option is a that this effect arises from a nonlinear effect. Such a nonlinear effect can explain an energy transfer from the PhPs to other material excitations, such as effective dipole emitters of hBN defects, or other phononic modes influenced by the sample size.

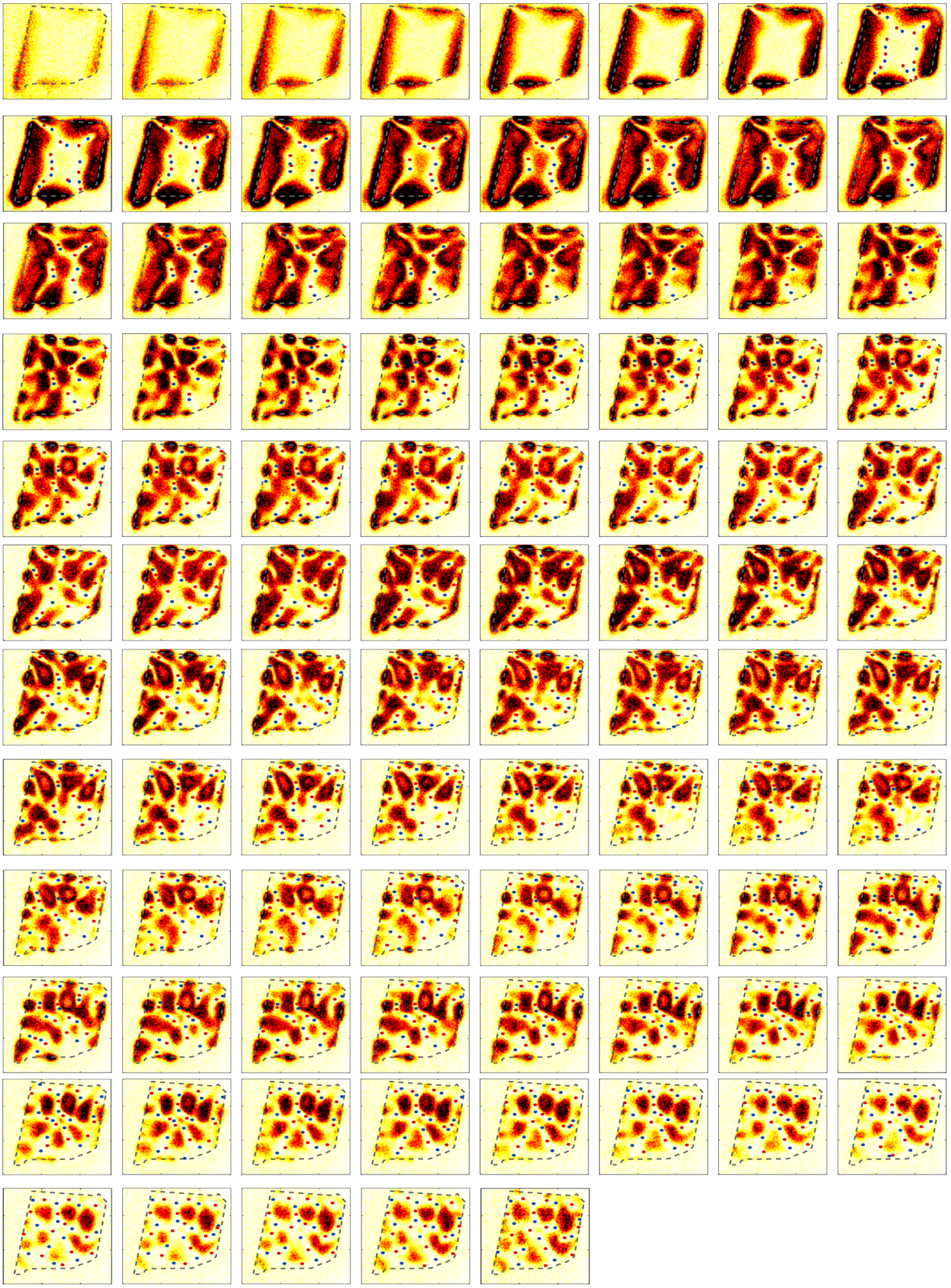

Figure S1: Recoded field maps showing the spatiotemporal dynamics, estimating the vortex location in each measurement. The vortices are created and annihilated according to the rules in Fig. 3 and form amplitude structures according to the rules in Fig. 4. This figure includes the complete measurement dataset (93 frames) with timestep of 50 fs between each frame.

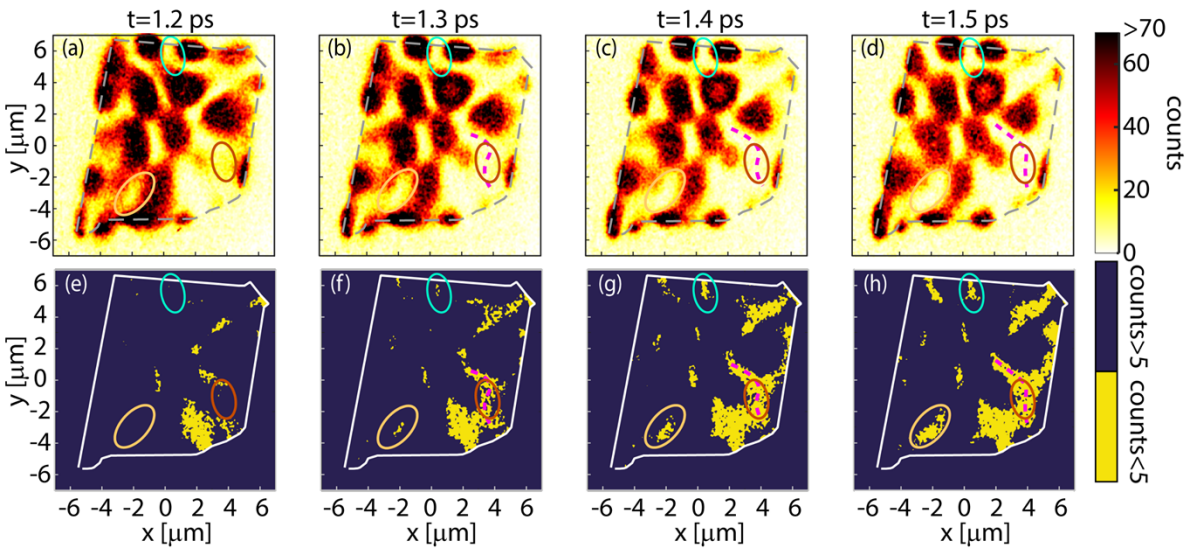

Figure S2: Experimental signature of vortex creation events. (a-d) The measured counts for different time delays. **(e-h)** The areas where optical vortices may appear in the images (a-d) are denoted in yellow. The single, and pair, vortex creation processes are identified and circled – pair creation from a nodal point (top left, yellow), a single vortex enters the sample (right edge, cyan), and pair creation along a nodal line (bottom left, red).

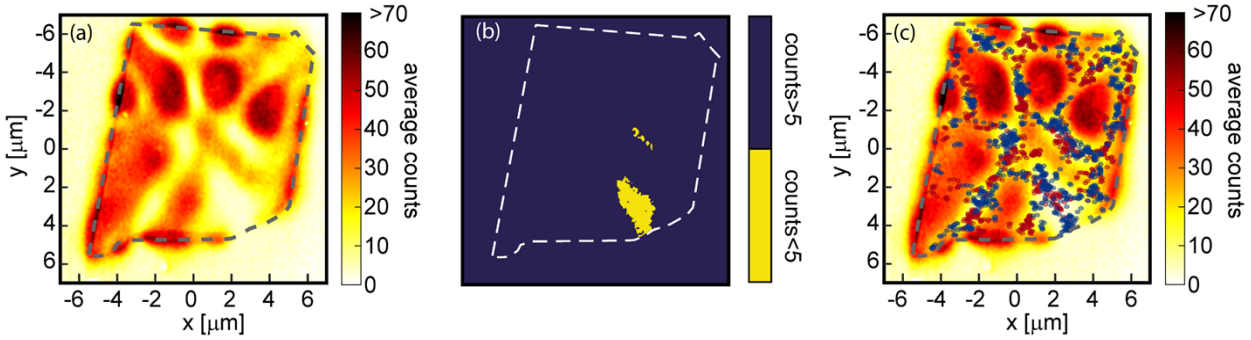

Figure S3: The accumulated signal, showing the robustness of nodal lines and nodal points. **(a)** The field amplitude map averaged over the entire measurement duration, showing that certain nodal lines remain approximately fixed in place throughout the entire measurement. **(b)** The areas in the average signal with less than 5 counts. Thus, apart from the two-colored areas, all other vortices and nodal lines move in time. **(c)** The same image as (a) but marking all the vortices we recognized throughout the measurement (at all timeframes). This image shows that although the vortices are dynamical, they moved according to specific trajectories, accumulated near specific nodal lines and nodal points that are determined by the electromagnetic eigenmode of the structure at the central excitation wavelength.

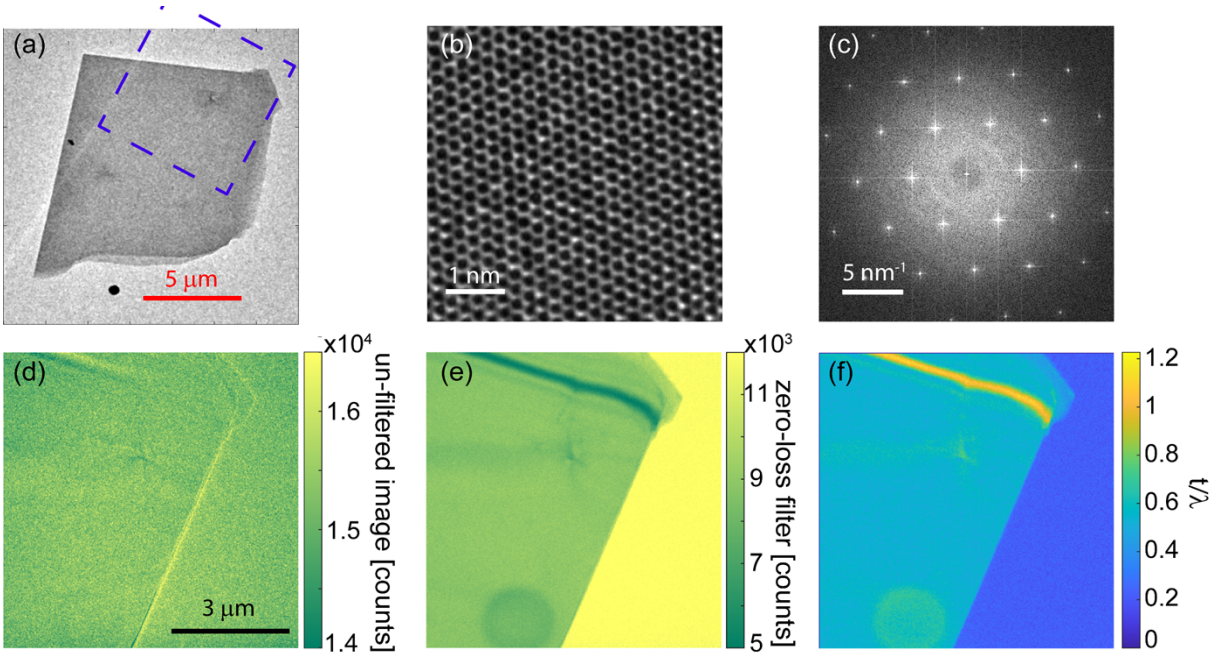

Figure S4: Sample analysis. (a) Grayscale image of the $h^{10}BN$ sample, exfoliated on a 20 nm Si_3N_4 membrane. The blue dashed square denotes the area of analysis in panels (d-f). **(b)** Zoom-in of the hBN lattice. **(c)** The FFT of (b), showing a clear hexagonal periodicity. **(d)** Un-filtered image of the sample and the membrane which includes electrons of all energies (similar as (a)). **(e)** An energy filtered image that includes only the zero-loss peak electrons. That is, the image excludes all electrons that performed inelastic scattering. **(f)** The ratio t/λ (thickness over the mean free path) which equals the log ratio between images (d) and (e). From this image, we find that the Si_3N_4 thickness is 19.531 ± 0.0015 nm and that the $h^{10}BN$ thickness is 40.3 ± 0.22 nm in its main area. The sample has local defects such as the circle-shape with thickness of 53 ± 0.6 nm and a line with thickness of 110 ± 5 nm.

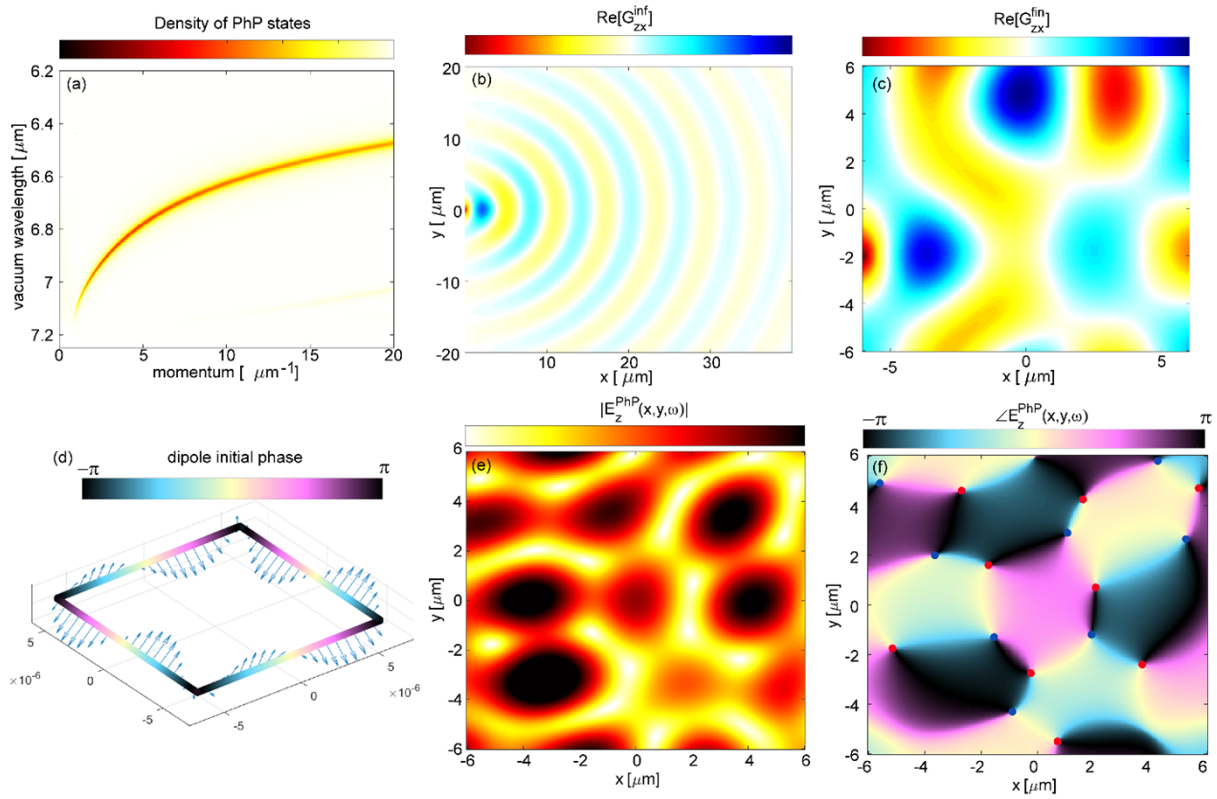

Figure S5: Simulating the PhP vortex dynamics. (a) The local density photonic states (LDOS) for the PhP modes in a 40 nm $h^{10}BN$ flake on top of a 20 nm Si_3N_4 membrane, described through Im (r_p). **(b)** The real part of the z-x component of the Green's function for an infinite slab in the x-y plane, in a frequency of $\omega = \frac{2\pi c}{7.1\ \mu m}$ $\mathrm{Re}(G_{zx}^{\mathrm{inf}}(x,y;0,0;\ \omega = \frac{2\pi c}{7.1\ \mu m}))$. **(c)** The real part of the z-x component of the Green's function for a 6×6 μm^2 sample as a result of a dipole located at $(-6\ \mu m, -2\ \mu m)$ with a frequency of $\omega = \frac{2\pi c}{7.1\ \mu m}$ $\mathrm{Re}(G_{zx}^{\mathrm{inf}}(x,y;0,0;\ \omega = \frac{2\pi c}{7.1\ \mu m}))$. **(d)** The relative phase (color) and real part of the induced dipoles on the edge of the sample excited by a 7.1 μm laser arriving at $\theta = 60°, \phi = 45°$ and polarization of $\alpha = 45°$. **(e)** The absolute value of the PhP field's z-component following the excitation from (d). **(f)** The phase of the field from (e) with the vortices in the location of the green and red dots.

Figure S6: Vortex spatiotemporal dynamics in COMSOL simulations. The amplitude (top panels) and phase (bottom panels) of the electric field z-component for different timeframes. The excitation's center wavelength is 7.25 μm and FWHM is 1 μm (temporal FWHM of 500 fs), impinging from an angle of 65° above the plane of the flake (135° in the *x*-*y* plane, anti-clockwise from the x axis). We find a similar qualitative behavior of the field amplitude as we find in the experiment. Moreover, we verify that the similar annihilation and creation rules are found also in these simulations. Interestingly, the spatiotemporal vortex dynamics in this simulation and in the measurement all change more slowly than in the square simulation due to the chaotic boundary conditions that force fewer eigenmodes in the system for a given bandwidth (*12*). The full video of the simulation can be found in Movie S4.

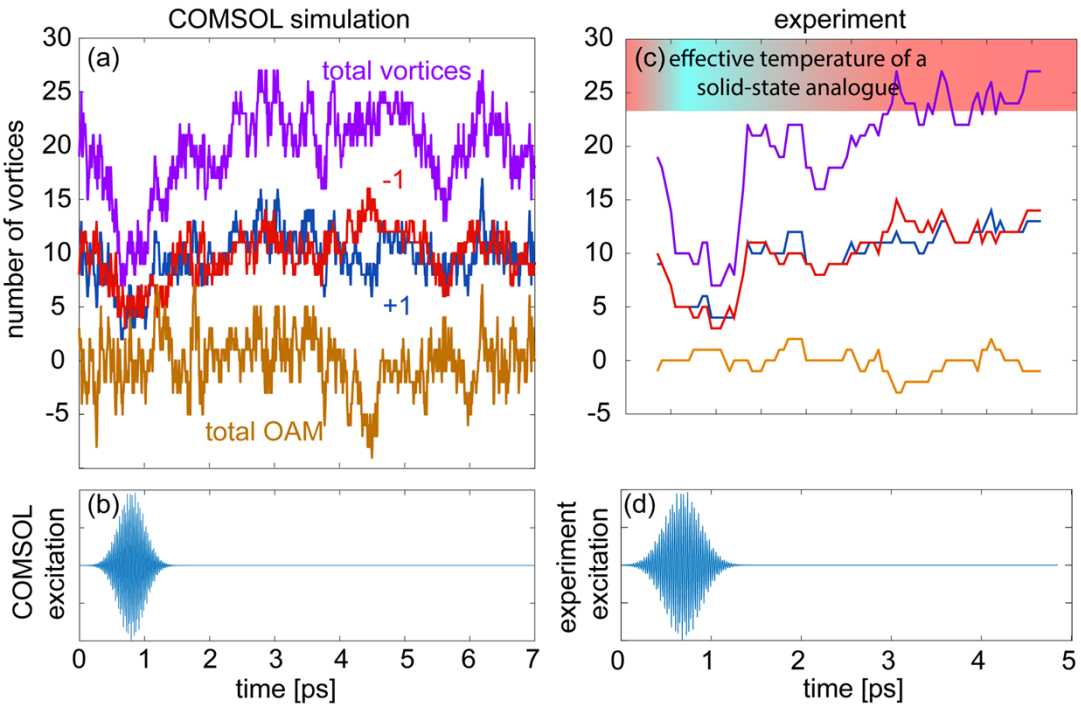

Figure S7: Tracking the total number of vortices and the total OAM. Comparison of the COMSOL simulations and the experiment, showing the same qualitative features in both. During the laser excitation, the number of vortices gradually reduces and then increases again after the excitation ends. This behavior suggest that the laser brings order to the system, in an analogue to the low-temperature order that reduces the number of vortices in solid-state systems. This finding inspires ideas for using optical vortices to simulate phase-transition phenomena of solid-state systems. A false-color scheme of this temperature analogue is shown in red. **(a)** The number of vortices with an OAM of +1 (blue), -1 (red), their sum (purple), and difference (brown). Importantly, the total OAM according to this count (brown) equals the total OAM of the sample if integrating over the PhP phase along the sample's edge. We find that none of the quantities remain constant in time: the total OAM changes due to creation or annihilation of vortices on the edges,

and the total number of vortices change also due to pair creation of annihilation. **(b)** The excitation of the COMSOL simulation, with a FWHM of 500 fs. **(c)** The measured number of vortices (with similar color scheme as (a)), showing a qualitative match to the trends predicted in the simulations regarding the total number of vortices and total OAM. **(d)** The expected excitation field extracted from the measurement.

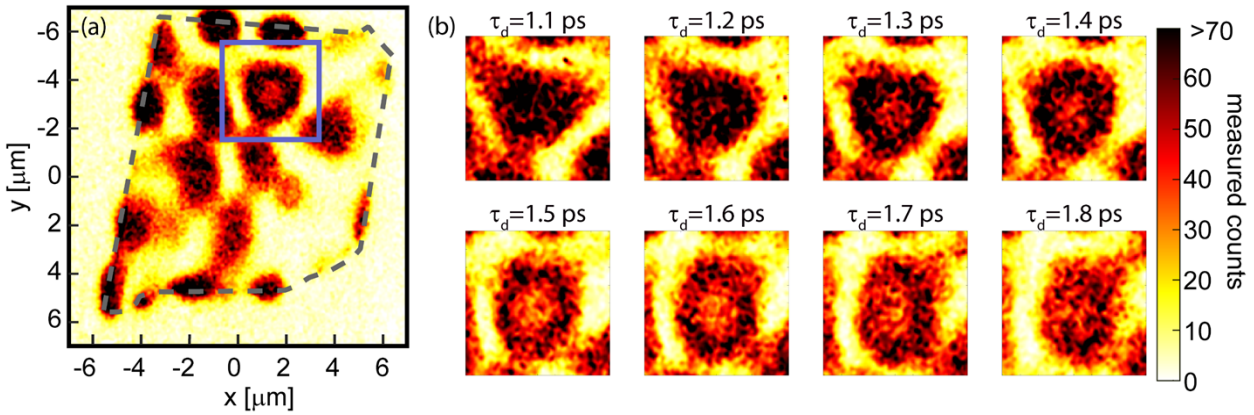

Figure S8: A PhP ring. (a) A measured snapshot. The dashed square indicates the area where the surprising ring is formed. **(b)** The spatiotemporal dynamics reveals the appearance and subsequent disappearance of the ring.

Movie S1: Measurement of the energy-filtered electrons as a function of time delay. The measurement shows the continuous change of the PhP dynamical interference patterns, and therefore a continuous change in the nodal points (areas of zero counts). The dashed gray contour is the sample's edge.

Movie S2: Simulated PhP dynamics in a square sample. (a-b) Amplitude $|E_z|$ and phase $\angle E_z$ of the PhP field in a 6X6 μm^2 40-nm thick hBN sample. The simulation verify that the nodal points indeed correspond to optical vortices. **(c)** The laser excitation amplitude in time. The laser arrives from the x-axes, at an angle of 65° above the sample, and a polarization of 45°. **(d)** Denoting the areas from (a) with significantly low amplitudes. We see that the vortices are allocated in these areas alone.

Movie S3: Automated identification of optical vortices, marked on Movie S1. The vortices are allocated according to the creation and annihilation rules from Fig. 3, the rules of field amplitude distribution from Fig. 4a-b, and the process of detecting vortex creation processes from Fig. S2. All frames of the Movie are also shown in Fig. S1.

Movie S4: Simulated PhP dynamics using COMSOL. (a-b) Amplitude $|E_z|$ and phase $\angle E_z$ of the PhP field in 40-nm thick hBN sample of dimensions similar to the sample in the experiment (shown in Fig. S6). We extract from COMSOL the frequency response of the structure in response to monochromatic excitations, and convert a range of such simulations to the time domain in a weighted manner: $\boldsymbol{E}_{\mathrm{PhP}}(x,y;t) = \mathcal{F}^{-1}\{\boldsymbol{E}_{\mathrm{COMSOL}}(\boldsymbol{r};\omega)\mathcal{F}\{A_{\mathrm{ext}}(t)\}\}$, where $\boldsymbol{E}_{\mathrm{COMSOL}}(\boldsymbol{r};\omega)$ is the COMSOL PhP electric field and A_{ext} is the excitation amplitude in time that we determine to match the experimental excitation (FWHM of 400 fs, shown in (c)). **(c)** The temporal properties of the excitation laser. **(d)** The areas from (a) with significantly low amplitudes. We use this COMSOL simulation to provide another verification of the creation and annihilation rules, highlighting the connection between the field amplitude and the vortex locations.

References

1. Y. Kurman, R. Dahan, H. H. Sheinfux, K. Wang, M. Yannai, Y. Adiv, O. Reinhardt, L. H. G. Tizei, S. Y. Woo, J. Li, J. H. Edgar, M. Kociak, F. H. L. Koppens, I. Kaminer, Spatiotemporal imaging of 2D polariton wave packet dynamics using free electrons. *Science (80-.).* **372**, 1181–1186 (2021).
2. F. J. Garcia De Abajo, A. Asenjo-Garcia, M. Kociak, Multiphoton absorption and emission by interaction of swift electrons with evanescent light fields. *Nano Lett.* **10**, 1859–1863 (2010).
3. S. T. Park, M. Lin, A. H. Zewail, Photon-induced near-field electron microscopy (PINEM): theoretical and experimental. *New J. Phys.* **12**, 123028 (2010).
4. O. Reinhardt, I. Kaminer, Theory of Shaping Electron Wavepackets with Light. *ACS Photonics*. **7**, 2859–2870 (2020).
5. E. J. C. Dias, F. J. García De Abajo, Fundamental Limits to the Coupling between Light and 2D Polaritons by Small Scatterers. *ACS Nano*. **13**, 5184–5197 (2019).
6. J. H. Kang, S. Wang, Z. Shi, W. Zhao, E. Yablonovitch, F. Wang, Goos-Hänchen Shift and Even-Odd Peak Oscillations in Edge-Reflections of Surface Polaritons in Atomically Thin Crystals. *Nano Lett.* **17**, 1768–1774 (2017).
7. M. Tamagnone, A. Ambrosio, K. Chaudhary, L. A. Jauregui, P. Kim, W. L. Wilson, F. Capasso, Ultra-confined mid-infrared resonant phonon polaritons in van der Waals nanostructures. *Sci. Adv.* **4**, 4–10 (2018).
8. S. Liu, R. He, L. Xue, J. Li, B. Liu, J. H. Edgar, Single Crystal Growth of Millimeter-Sized Monoisotopic Hexagonal Boron Nitride. *Chem. Mater.* **30**, 6222–6225 (2018).
9. N. Hadji, Detailed Electron Energy Loss Spectroscopy (EELS) Microanalysis of Data Collected Under Semi-Angle Less Than Both Plasmon Cutoff Angle and Incident Beam Convergence Semi-Angle, 1–18 (2020).
10. H. Shinotsuka, S. Tanuma, C. J. Powell, D. R. Penn, Calculations of electron inelastic mean free paths . XII . Data for the full Penn algorithm . **51**, 427–457 (2018).
11. J. F. NYE, M. V. BERRY, Dislocations in wave trains. *Proc. R. Soc. London. A. Math. Phys. Sci.* **336**, 165–190 (1974).
12. I. Freund, Optical vortices in Gaussian random wave fields: statistical probability densities. *J. Opt. Soc. Am. A*. **11**, 1644 (1994).